Global Orientation of Bound MMP-3 and N-TIMP-1 in Solution via Residual Dipolar Couplings[†,‡]

S. Arumugam[§] and Steven R. Van Doren*

Department of Biochemistry, 117 Schweitzer Hall, University of Missouri, Columbia, Missouri 65211

Received April 7, 2003; Revised Manuscript Received May 17, 2003

ABSTRACT: Crystal structures of catalytic domains of MMP-3 and MT1-MMP bound to TIMP-1 or TIMP-2, respectively, differ in the orientation of the TIMP in the MMP active site. The orientation in solution of N-TIMP-1 in the MMP-3 active site has been investigated using residual dipolar couplings (RDCs). Fitting of the RDCs to the X-ray structures of the complexes suggests general agreement with the orientation of crystalline MMP-3(ΔC) and TIMP-1 and a large disparity from the orientation of crystalline MT1-MMP(ΔC) and TIMP-2. Rigid body docking of MMP-3 and N-TIMP-1 X-ray coordinates using RDCs and intermolecular NOEs provided a time-averaged orientation in solution differing from the crystal structure by a 5° rotation toward the MT1-MMP(ΔC)/TIMP-2 orientation. The slight discrepancy in orientations in solution and crystal lies within the experimental uncertainties. Intermolecular NOEs used in the docking corroborated the accuracy of mapping the interface by a paramagnetic NMR footprinting assay, a potential alternative source of contacts for docking. Some uncertainty in the N-TIMP-1 orientation in the MMP-3 active site, coupled with microsecond to millisecond fluctuations of the MMP-binding ridge of N-TIMP-1 in the complex and flexibility in MMP-3(ΔC) S_1' to S_3' subsites, leaves open the possibility that N-TIMP-1 might dynamically pivot a few degrees or more in the arc toward the MT1-MMP(ΔC)/TIMP-2 orientation. Differing TIMP orientations in MMP active sites are more likely to result from structural differences in TIMP AB hairpin loops than from crystal packing artifacts.

TIMP-1[1] and TIMP-2 were reported to orient differently in matrix metalloproteinase active sites (*1*). Matrix metalloproteinases (MMPs) are zinc endopeptidases that act on extracellular matrix proteins during the connective tissue remodeling of development, reproduction, wound healing, cancer, arthritis, and other tissue degenerative diseases. Such activities of MMPs are inhibited by 1:1 molar binding by endogenous tissue inhibitors of metalloproteinases (TIMPs) -1, -2, -3, or -4, typically with subnanomolar K_I values (*2*, *3*). The presence of TIMPs inversely correlates with oncogenicity (*4*). Transgenic overexpression of MMP-3 in mice stimulates the development of mammary tumors in mice, unless TIMP-1 is coexpressed (*5*).

The N-terminal two-thirds of human TIMPs-1 or -2 (N-TIMP-1 or -2) are sufficient to fold (*6*) with much better yield than full-length and to inhibit MMPs-1, -2, and -3 with K_I values of 1−2 nM (*7*). The difference in K_I of 1.4 nM for N-TIMP-1 inhibition of MMP-3 from K_I of 0.22 nM for full-length TIMP-1 inhibition of MMP-3 represents a $\Delta\Delta G_I$ of only 1.1 kcal/mol (i.e., 9% of ΔG_I (*7*)). N-TIMP-1 is being engineered to increase its selectivity among MMPs (*8*−*10*), a sought-after property for decreasing side effects of potentially therapeutic MMP inhibitors. Likewise, N-TIMP-2, -3, and -4 are being successfully engineered for greater selectivity among metalloproteinases (*10*−*13*). Because of the therapeutic potential of engineered N-TIMPs for treating cancer and arthritis, better understanding of the MMP-binding mode of N-TIMP-1 is sought. High-precision NMR structures of N-TIMP-2 and N-TIMP-1 show that they comprise β-strands A−F in a sheared barrel of the OB-fold, with helices 1 and 2 on one side of the β-barrel (*14*, *15*). MMP-3(ΔC) comprises β-strands I−V and helices A−C (*16*). The backbone dynamics of N-TIMP-2 and N-TIMP-1, free and bound to the catalytic domain of MMP-3 (MMP-3(ΔC)), have been characterized (*17*−*19*). Contrary to prediction, tight binding of MMP-3(ΔC) by N-TIMP-1 is endothermic. Interestingly, part of the substantial favorable entropic free energy of binding appears to arise from conformational entropy gain introduced through much of the β-barrel of N-TIMP-1 by binding of MMP-3(ΔC) (*19*).

X-ray structures are available for MMP-3 bound to TIMP-1 (*20*) and for MT1-MMP bound to TIMP-2 (*1*). With the MMP catalytic domains of these structures superimposed, TIMP-1 and TIMP-2 differ in orientation in the MMP active site by 20, 10, and 5° rotations about orthogonal axes centered on TIMP residue 4 (*1*). This raises the question of the reason(s) for differing orientations in similar MMP active

[†] This work was supported by DHHS Award GM57289 to S.R.V.

[‡] Coordinates of the apparent average orientation in solution have been deposited in the Protein Data Bank at www.rcsb.org/pdb/ under accession code 1oo9 for release upon publication.

* To whom correspondence should be addressed. Tel.: (573) 882-5113. Fax: (573) 884-4812. E-mail: vandorens@missouri.edu.

[§] Current address: James Graham Brown Cancer Center, 529 S. Jackson St., University of Louisville, Louisville, KY 40202.

[1] Abbreviations: IPAP, in-phase, anti-phase; MMP, matrix metalloproteinase; MMP-3, stromelysin 1; MMP (ΔC), MMP catalytic domain, lacking C-terminal domain; MT1-MMP, membrane type 1 MMP; NOE, nuclear Overhauser enhancement; RDC, residual dipolar coupling; SVD, singular value decomposition; TIMP, tissue inhibitor of metalloproteinases; N-TIMP-1, N-terminal MMP-inhibitory domain of TIMP-1.

10.1021/bi034545s CCC: $25.00
Published on Web 06/12/2003

sites. Contributors to the differing orientation possibly include differences in the AB loop of the TIMPs, inherent flexibility in the thin MMP-binding ridge of the TIMPs, differences in the strand V to helix B loop of the MMPs, and perturbation by crystal packing effects. Using residual dipolar couplings (RDCs) measured from weakly aligned samples (*21*), solution NMR can accurately correct long-range orientations of protein complexes (*22*−*25*), domains (*26*, *27*), and other biomolecular assemblies (*28*−*30*) in solution. We find that in solution, the apparent average orientation of N-TIMP-1 in the MMP-3(ΔC) active site agrees within the uncertainty with the crystal structure of the complex of TIMP-1 with MMP-3(ΔC). This suggests that the crystalline orientation is not significantly skewed by crystal packing and that the reported difference in TIMP-1 and TIMP-2 in MMP active sites is more likely to be a consequence of structural differences such as those in the AB loops of TIMPs.

EXPERIMENTAL PROCEDURES

Assignment of NMR Peaks of Complex of MMP-3(ΔC) with N-TIMP-1. To stabilize the complex of human MMP-3(ΔC) with N-TIMP-1 for NMR, an E202Q substitution in the MMP-3 active site was introduced (*19*) that preserves TIMP binding (*31*, *32*) and the structure of MMP-3(ΔC) (*33*). Details of preparing a homogeneous 1:1 complex and assignments of the backbone NMR peaks of N-TIMP-1 in the complex were described (*19*). Backbone assignments of the MMP-3(ΔC) bound to N-TIMP-1 were obtained previously (*19*, *34*). Conditions for NMR were 307 K, 20 mM Tris-d_{11}, pH 6.22, 125 mM NaCl, 10 mM $CaCl_2$, 1 mM NaN_3, and 50 μM $ZnCl_2$. Side chain assignments of the MMP-3(ΔC) component of the complex in 90% H_2O relied on HCCH-COSY, HCCH-TOCSY, HCACO, and HNCO. Assignments of MMP-3(ΔC) bound to a synthetic inhibitor (*35*, *36*) also aided assignment of MMP-3(ΔC) when bound to N-TIMP-1. About 80% of side chain assignments of MMP-3(ΔC) E202Q in the complex were completed and deposited together with MMP-3(ΔC) backbone assignments at BioMagResBank under accession code 5785. Missing side chain assignments were due either to severe overlap or broadening of methylene peaks. A similar strategy was used to assign the side chains of N-TIMP-1 in complex with MMP-3(ΔC) E202Q. However, for $^{15}N/^{13}C$ N-TIMP-1 or $^{15}N/^{13}C/50\%$ ^{2}H N-TIMP-1 bound to unlabeled MMP-3(ΔC) E202Q, CBCA(CO)NH, C(CO)NH, and H(C)(CO)NH spectra were mostly incomplete, perhaps because of greater chemical exchange broadening of the lines of the N-TIMP-1 component of the complex (*19*). As a result, HCCH-TOCSY and ^{15}N-separated NOESY, aided by assignments of free N-TIMP-1, were most fruitful for assigning nearly 70% of the side chains of N-TIMP-1 when bound to MMP-3(ΔC) E202Q. These assignments have been deposited under BMRB accession code 5099.

Measurement and Fitting of RDCs for Use in Orienting the Complex. To measure RDCs, N-TIMP-1 was labeled with $^{2}H/^{15}N$ and bound 1:1 to MMP-3(ΔC) E202Q as reported (*19*). The MMP-3(ΔC) E202Q component of this complex was selectively labeled with ^{15}N Ile, ^{15}N Val, and $^{15}N/^{13}C$ Leu that were part of a defined medium with the 17 other amino acids being unlabeled, similar to a previous selective labeling (*35*). A mixture of 5% PEG C12E6 with 1-hexanol at a molar ratio of 0.64 (*37*) was used to align a 0.17 mM complex of $^{2}H/^{15}N$ N-TIMP-1 with ^{15}N I/V/L MMP-3(ΔC) E202Q for collection of IPAP-HSQC spectra (*38*, *39*). RDCs ranged as high as several tens of Hz, as evident from Figure 1A. Powder pattern analysis of a histogram of the $^{1}D_{NH}$ and

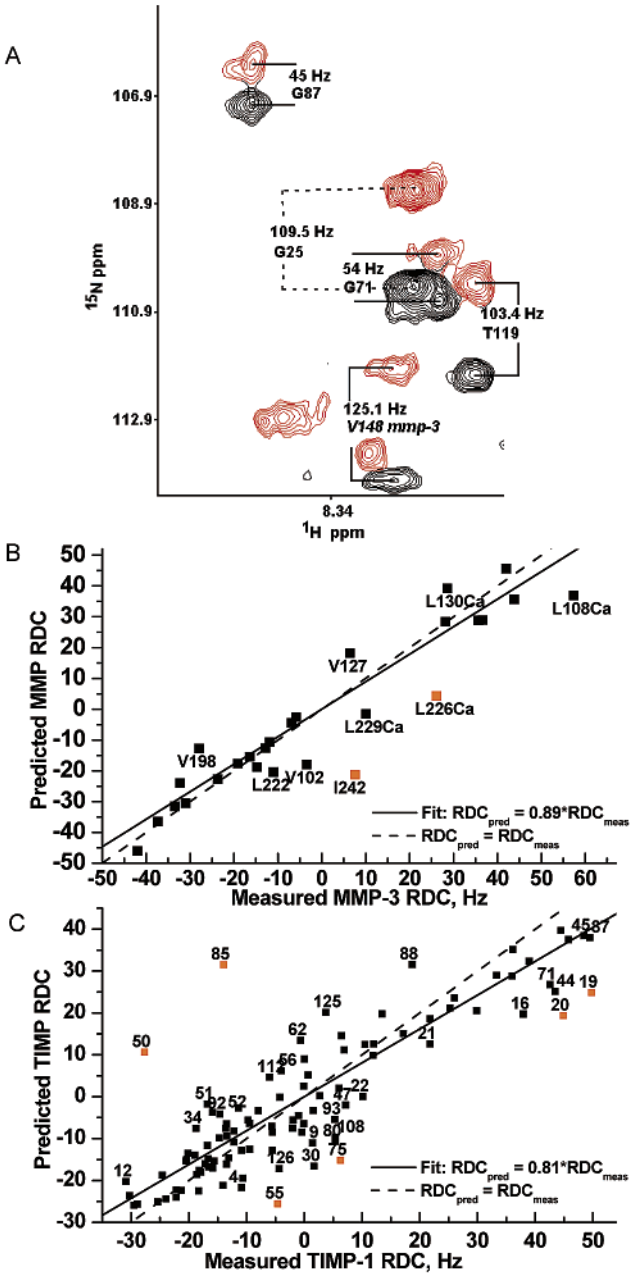

FIGURE 1: Amide RDCs of the complex of MMP-3(ΔC) with N-TIMP-1 used for reorientation of X-ray coordinates of each protein. (A) Overlay of sum and difference ^{15}N IPAP-HSQC subspectra (*38*, *39*), specifically a region showing RDCs with a range of amplitudes. The upfield component of each doublet is shown with red contours. (B) $^{1}D_{NH}$ and $^{1}D_{C\alpha H}$ RDCs calculated for MMP-3(ΔC), using PDB coordinates 1uea chain A, are plotted against the RDCs measured in solution. (C) $^{1}D_{NH}$ RDCs calculated for TIMP-1, using chain B of 1uea, are plotted against RDCs measured for N-TIMP-1 in solution. (B and C) The predicted values were calculated from best fits to individual chains of the crystal structure using singular value decomposition (SVD) implemented in Module (*29*). RDC measurements differing by at least 9 Hz from the SVD prediction from the X-ray structure are labeled with residue numbers. Measured RDCs differing by 21 Hz or more from the SVD prediction are marked with orange squares and were omitted both from calculation of alignment tensors displayed in Figure S1 of Supporting Information and from the evaluations of Table 1.

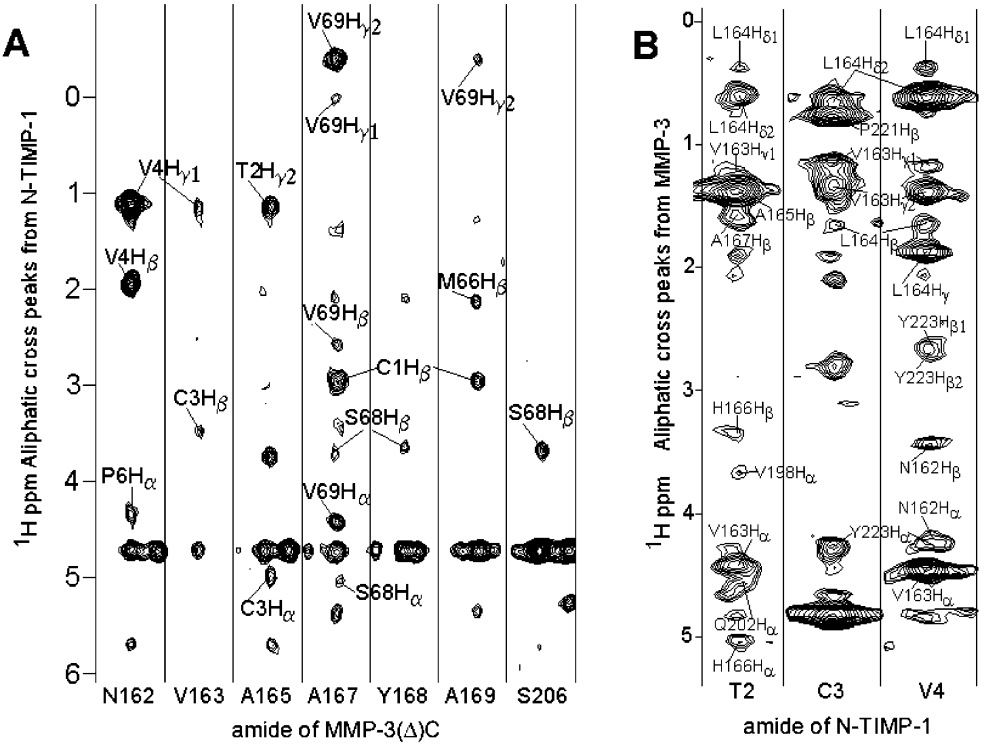

FIGURE 2: NOEs between MMP-3(ΔC) and N-TIMP-1 used for rigid body docking. (A) Skewers from ^{15}N-separated NOESY of ^{2}H/^{15}N-labeled MMP-3(ΔC) bound to unlabeled N-TIMP-1. N-TIMP-1 side chain assignments appear next to cross-peaks. (B) Skewers from ^{15}N-separated NOESY of ^{2}H/^{15}N-labeled N-TIMP-1 bound to unlabeled MMP-3(ΔC). MMP-3(ΔC) side chain assignments appear next to cross-peaks.

$^1D_{H\alpha C\alpha}$ RDCs (*40*) suggested the Da parameter, describing the degree of alignment along the principal longitudinal alignment axis, to be 24.8 Hz, with respect to $^1D_{NH}$ values. Rhombicity values, *R*, ranging from 0.20 to 0.25 were obtained from fits of RDCs to structural coordinates using singular value decomposition (SVD) implemented in either PALES (*41*) or Module (*29*). Alignment tensors were visualized using Module.

NOE Contacts between MMP-3(ΔC) and N-TIMP-1. Preparation of samples of the complex in which one protein was uniformly enriched with ^{15}N/^{2}H to >97%, while the partner was unlabeled, enabled measurement of intermolecular NOEs between aliphatic protons of the unlabeled protein and amide protons of the ^{15}N/^{2}H-labeled partner (amide protons that returned by exchange during purification). ^{15}N-separated NOESY-HSQC spectra (*42*) of the free proteins did not produce any cross-peaks in the aliphatic region, confirming their full deuteration. By contrast, ^{15}N NOESY-HSQC spectra of the complexes of ^{15}N/^{2}H MMP-3(ΔC) E202Q with unlabeled N-TIMP-1 and of unlabeled MMP-3(ΔC) E202Q with ^{15}N/^{2}H N-TIMP-1, obtained with mixing times of 220 and 250 ms, respectively, showed cross-peaks in the range of −0.7−5.7 ppm in the indirect ^{1}H dimension (vertical ^{1}H scale of Figure 3). The perdeuteration of aliphatic and aromatic groups decreased spin-diffusion in the detected amide spectrum during the long mixing times.

Computation of Orientation of N-TIMP-1 in MMP-3(ΔC) Active Site in Solution. XPLOR-NIH (*43*) was used for rigid body redocking of human MMP-3(ΔC) and the N-terminal 126 residues of human TIMP-1 (N-TIMP-1) from X-ray coordinates of the complex (PDB accession code 1uea (*20*)). While crystallography used substitutions of selenomethionine and N30A and N78A lesions in TIMP-1 (*20*), the solution NMR herein used the wild-type N-TIMP-1 sequence. As discussed below, 46 intermolecular NOEs, 75 $^1D_{NH}$ RDCs of N-TIMP-1, 19 $^1D_{NH}$ RDCs of MMP-3(ΔC) E202Q, and eight $^1D_{H\alpha C\alpha}$ RDCs of MMP-3(ΔC) E202Q were used for solution docking. Starting structures were generated by rigid body minimization (*22*) and followed by restrained Cartesian simulated annealing in which the backbone was kept rigid by restraining to a duplicate molecule using noncrystallographic symmetry as described (*23*). (A more computationally efficient docking procedure using conjoined rigid body/torsion angle dynamics has since become available but was not used (*44*, *45*).) Interfacial side chains of the following residues were allowed to be flexible during the simulation: 162−169, 198−202, 205−206, 211, and 221−223 of MMP-3(ΔC); 302−304, 329, 333−335, and 366−369 of N-TIMP-1 (for convenience in the PDB file, 300 has been added to the normal TIMP-1 numbering). The target functions included terms for NOE-derived restraints, RDC restraints, and the radius of gyration. Interfacial contacts in structural models of the complex were compared using solvent accessibilities measured with NACCESS v2.1.1, available from http://wolf.bms.umist.ac.uk/naccess/.

N-TIMP-1 Binding Surface and Depth Dependence of MMP-3(ΔC) Line Broadening by Gd-EDTA. Line broadening of protons (i.e., T_2^{-1}) below a surface with nonspecific collisions with a paramagnetic ion can be modeled by a simplification of the Solomon−Bloembergen expression:

$$\frac{1}{T_2} \propto \frac{\gamma_H{}^2\beta^2 S(S+1)}{r^6}\tau_c$$

where *r* is the distance between proton and a paramagnetic

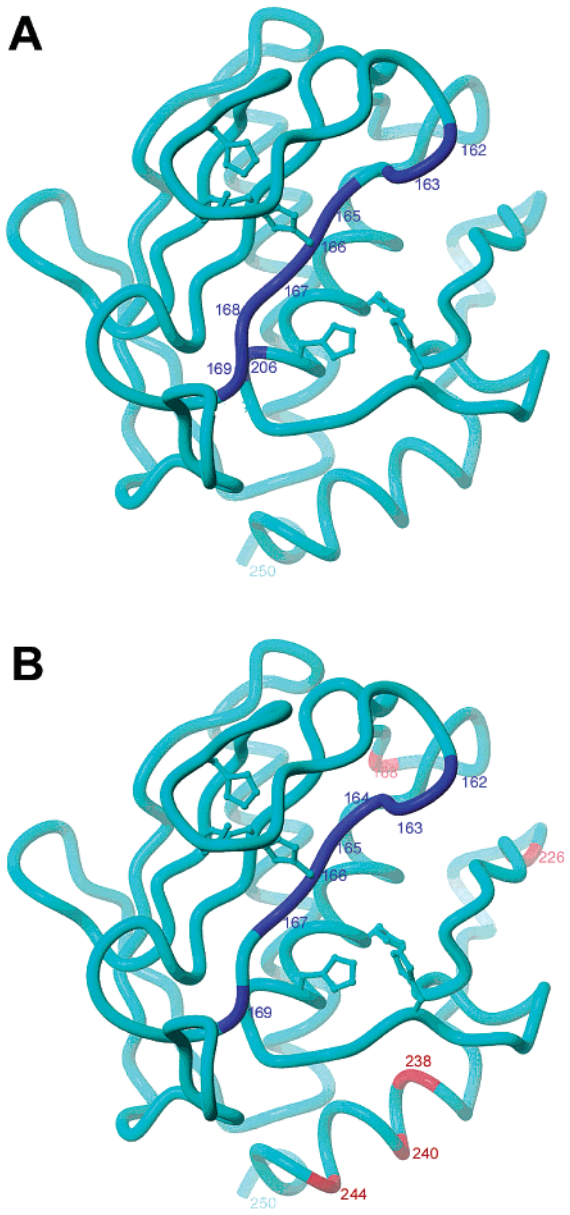

FIGURE 3: Sites of contact of N-TIMP-1 with the MMP-3(ΔC) backbone confirm the accuracy of protection from line broadening by chelated Gd(III) in mapping this interface. (A) MMP-3(ΔC) residues whose amide groups manifest intermolecular NOEs to N-TIMP-1 (Figure 2A) are colored dark blue and numbered. (B) MMP-3(ΔC) residues most protected by N-TIMP-1 binding from line broadening by a Gd-EDTA probe are marked dark blue and numbered (*34*). Those residues that become more exposed to the line broadening effects of the Gd-EDTA probe upon N-TIMP-1 binding, because of displacement of the MMP-3(ΔC) N-terminus from its C helix due to TIMP-1 binding, are colored red (*34*).

center, and β is the Bohr magneton. The large value of γ_H, the proton gyromagnetic ratio, makes proton lines especially sensitive to broadening. Since chelated Gd(III) has $S = 7/2$, it is especially effective at relaxing proton lines, making it a successful MRI contrast agent (*46*). The N-TIMP-1-dependence of MMP-3(ΔC) amide proton line broadening by Gd-EDTA was assayed (*34*). Exposure of uninhibited ^{15}N-enriched MMP-3(ΔC) to 3 mM Gd-EDTA attenuated HSQC peak heights to a similar degree as exposure of the MMP-3(ΔC) bound to N-TIMP-1 to 2 mM Gd-EDTA, judging from peaks of residues far from the catalytic cleft. (The lower [Gd-EDTA] used with the complex is due to its being more sensitive to the broadening, because of the slower tumbling of the complex that increases τ_c in the expression above). The peak heights were normalized by the peak heights prior to addition of Gd-EDTA. For comparison, the depth of amide protons below the nearest Gd-EDTA accessible surface of uninhibited MMP-3(ΔC) and MMP-3(ΔC) with N-TIMP-1 bound was analyzed. Gd-EDTA accessible surfaces were modeled using GRASP (*47*) using a probe radius of 4 Å to represent the Gd-EDTA. To represent N-TIMP-1, the C-terminal domain of TIMP-1 was removed from X-ray coordinates of the complex (PDB code 1uea) (*20*). The small *N*-carboxy alkyl inhibitor was removed from X-ray coordinates of MMP-3(ΔC) (PDB code 1sln) (*48*) to represent its free state. For measuring depth, protons were added to the two X-ray models.

RESULTS AND DISCUSSION

Measurement of Residual Dipolar Couplings. Specific labeling of the valine, isoleucine, and leucine residues of MMP-3(ΔC) E202Q was combined with uniform ^{15}N/^{2}H labeling of the N-TIMP-1 bound, followed by weak alignment with liquid crystals aligned in the magnetic field. This ensured an identical environment of alignment of the two proteins for measurement of RDCs used to orient them. The peaks of the hydrophobic residues of human MMP-3(ΔC) have enough spectral dispersion that their specific labeling did not introduce much spectral overlap. The weak alignment was homogeneous and stable throughout RDC measurements since the D_2O line was a sharp doublet with constant 22 Hz splitting at 305 K before and after each spectrum used to measure the RDCs of N−H and leucine C−H bonds. $^{1}D_{NH}$ RDCs of 102 residues of N-TIMP-1 and of 20 specifically labeled valine, isoleucine, and leucine residues of MMP-3(ΔC) were measured using IPAP-HSQC spectra of the single sample, both when tumbling isotropically as normal and when weakly aligned (Figure 1). Eight reliable $^{1}D_{HaCa}$ RDCs of leucines of the MMP-3(ΔC) component were also obtained.

Comparison of RDCs with the Crystal Structure. To evaluate consistency of the RDCs both with the global orientation of MMP-3(ΔC) and TIMP-1 in their crystalline complex and with the structure's individual bond orientations, the RDCs were fitted by SVD to the X-ray structure (*20*). Figure 1B shows the correlation between the 27 RDCs (19 $^{1}D_{NH}$ and eight $^{1}D_{HaCa}$ RDCs) of MMP-3(ΔC) with the RDCs calculated from the MMP-3(ΔC)/TIMP-1 crystal structure (chain A of PDB 1uea). Deviations of measured RDCs from those calculated from a structure can arise from either static or dynamic differences (*21*, *49*). Dynamic structural averaging over time scales ranging from picoseconds to several milliseconds can affect RDCs (*49*). Among MMP-3 residues with largest deviations between measurement and prediction from the crystal structure, the amide bonds of Val102, Leu222, Leu226, and Leu229 were reported to be comparatively flexible with S^2 order parameters <0.80 (*50*) in MMP-3(ΔC) with an inhibitor bound in the $S_1'-S_3'$ subsites (see BMRB code 4364). (TIMPs bind both S_1-S_3 and $S_1'-S_3'$ subsites.) With the small inhibitor in $S_1'-S_3'$ subsites, Val102, Val127, Leu130, Val198, and Leu222 displayed at least 1.8 Hz of exchange broadening termed R_{ex}, suggesting that they fluctuate on the microsecond to millisecond scale. Consequently, the deviating cases in the correlation of Figure

1B might result from dynamic averaging of the backbone at some or all of residues Val102, Val127, Leu130, Val198, Leu222, and Leu226 of MMP-3(ΔC) E202Q with N-TIMP-1 bound. Leu226 lies at a site that varies most among structures of MMPs. Since Val198, Leu222, and Leu226 are critical in forming the S_1' principal specificity pocket, it is possible that this portion of the right side of the MMP-3 active site retains some residual flexibility in the interface with N-TIMP-1.

The 102 $^1D_{NH}$ RDCs of N-TIMP-1 were fitted by SVD to the X-ray coordinates of TIMP-1 bound to MMP-3(ΔC) (chain B of PDB code 1uea) (*20*). The majority of the N-TIMP-1 residues from the complex having the larger deviations of measured RDCs from those predicted from this X-ray structure (Figure 1C) coincide with sites of relatively greater flexibility. This higher flexibility is suggested by the parameters S^2 (reporting picosecond to nanosecond motion) or R_{ex} (reporting fluctuations over microseconds to milliseconds) from model-free fits of ^{15}N relaxation (*19*). Such N-TIMP-1 residues include Ile19, Arg20, Asn30, Lys44, Gln50, Ala51, Leu52, Ala55, Tyr62, Gly71, Ser80, Ile85, Lys88, Leu108, Glu125, and Glu126 (Figure 1C).

Omitting the eight most deviant of these RDCs (orange in Figure 1B,C), alignment tensors were fitted independently to TIMP-1 (using 96 $^1D_{NH}$ RDCs) and MMP-3(ΔC) (using 25 RDCs) main chains of the X-ray structure. The resulting orientation of the principal axes (A_Z) of alignment of N-TIMP-1 and MMP-3(ΔC) differed by 10° (Figure S1 of Supporting Information), raising the question of whether the proteins' orientation in solution and crystal might differ.

Effects of Structural Uncertainty on Alignment Parameters. In principle, correlation plots of structurally predicted RDCs versus measured RDCs would be expected to have a slope of unity (dashed lines in Figure 1B,C). The slopes fitted are, however, less than 1.0 (solid lines in Figure 1B,C). This attenuation has been attributed to structural uncertainty (noise) that diminishes the apparent degree of alignment, Da (*51*). The slope of 0.81 of the RDC fit to the N-TIMP-1 component being smaller than the slope of 0.89 for the fit to the MMP-3(ΔC) component of the complex suggests the possibility of greater structural uncertainty in the TIMP-1 chain of the X-ray structure. From SVD fitting of $^1D_{NH}$ RDCs to the individual proteins in the crystal structure of the complex, Da appears to be 22.5 Hz for MMP-3(ΔC) and 18.4 Hz for N-TIMP-1. These underestimate the Da estimated from the powder pattern distribution of RDCs, which is 24.8 Hz (*52*). The underestimates of Da from SVD fits are also consistent with structural uncertainty in the X-ray coordinates (*51*). Because MMP-3(ΔC) binding appears to increase flexibility through much of N-TIMP-1 and its β-barrel core, with flexibility remaining in the interface (*19*), dynamic averaging is likely to contribute to the structural uncertainty of the TIMP-1 chain in the 2.8 Å crystallographic coordinates of the complex. This adds to static errors in the X-ray coordinates behind deviating RDCs. The MMP-binding-induced flexibility increases were observed on scales of picoseconds to nanoseconds and microseconds to milliseconds, with the possibility of motions also on other time scales (*19*).

Trimmed Set of RDCs for Orienting N-TIMP-1 and MMP-3 in Solution. $^1D_{NH}$ RDCs from disordered segments of the N-TIMP-1 backbone were excluded from docking calculations because low S^2 order parameters should systematically attenuate RDCs (*21*). Excluded from use in docking were the $^1D_{NH}$ values of sites in loops or termini with $S^2 < 0.65$ that imply picosecond to nanosecond fluctuations of significant amplitude, namely, N-TIMP-1 residues 49−58 of its BC loop, Arg75 from its CD loop, and Glu125 and Glu126 from its C-terminus (*19*). Also excluded from use in docking were $^1D_{NH}$ measurements differing from $^1D_{NH}$ calculated from the MMP-3(ΔC)/TIMP-1 X-ray structure by at least 13 Hz, implying either static or dynamic deviations from the crystal structure. These deviant $^1D_{NH}$ values are from N-TIMP-1 residues 9, 16, 19, 20, 30, 44, 62, 71, 80, 85, 88, and 108 and from MMP-3(ΔC) residues 123 and 242. Most of these N-TIMP-1 residues (i.e., Ile19, Arg20, Asn30, Lys44, Tyr62, Gly71, Ser80, Ile85, Lys88, and Leu108) display exchange broadening evidence of fluctuations on the scale of microseconds to milliseconds (*19*). Although measured $^1D_{NH}$ of Gly92 and Leu93 each deviate only by 10 Hz from prediction using X-ray coordinates 1uea, they were also omitted from rigid body docking because localized SVD fitting of sets of $^1D_{NH}$ values of N-TIMP-1 residues 89−94 of the X-ray coordinates showed a clear discrepancy for this segment of the backbone (*19*). The global orientations presented in Figure 4 and evaluated in Table 1 were obtained without use of the deviating $^1D_{NH}$ values listed above.

Intermolecular NOE-Derived Contacts for Docking. For docking and enhancement of the orientational information from RDCs, intermolecular NOEs across the interface were gathered from samples in which one protein was unlabeled, and the bound partner was ^{15}N-labeled and perdeuterated in its side chains. This resulted in the side chain to amide NOEs being intermolecular (Figure 2). Assignment of these intermolecular NOEs required side chain assignments of MMP-3(ΔC) and N-TIMP-1 in their complex that were obtained to about 80 and 70% completion, respectively. (Broad methylene peaks in this 34 kD, 299-residue complex were difficult to assign.) The MMP-3(ΔC)/TIMP-1 X-ray structure corroborated assignments of the intermolecular NOEs of Figure 2. The amide protons of MMP-3 residues in and near β-strand IV (i.e., Asn162, Val163, Ala165, Ala167, Tyr168, and Ala169, along with Ser206) are spatially close to the aliphatic side chains of N-TIMP-1 (Figure 2A). Thr2, Cys3, and Val4 of N-TIMP-1 insert in the right side of the active site (i.e., at the $S_1'-S_3'$ subsites) where they make contact with backbone and side chains of Asn162−Ala167 at β-strand IV of MMP-3, as well as with Val198 and Gln202 of the active site helix and Pro221 and Tyr223 of the lower rim of the MMP-3 active site (Figures 2 and 4). On the left side (i.e., S_1 and S_2 subsites of the MMP-3 active site), the backbone of Ala167−Ala169 and Ser206 contact the side chains of Met66, Ser68, and Val69 of the AB loop of N-TIMP-1 plus its Cys1 (Figure 2A).

Intermolecular NOEs Show Accuracy of Protection from Gd-EDTA in Mapping Interface. The intermolecular NOEs validate a paramagnetic NMR footprinting assay that was introduced to identify the surface of MMP-3(ΔC) that binds N-TIMP-1 (*34*). The assay employs binding-induced protection of the labeled protein's surface from line broadening by a chelated Gd(III) probe (*34*). The MMP-3(ΔC) amide groups with NOEs to N-TIMP-1 (Figure 2A) are marked on the structure of MMP-3(ΔC) (Figure 3A). With remarkable

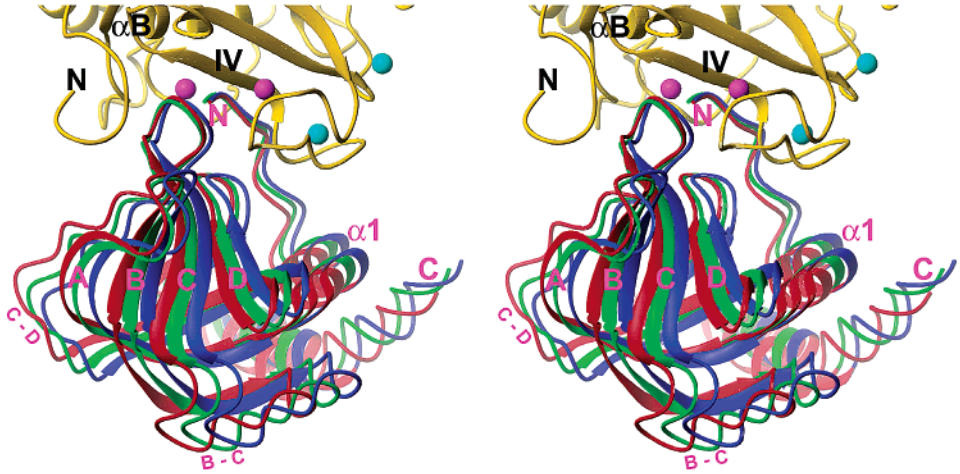

FIGURE 4: Superposition of crystal coordinates (TIMP-1 in red) with rigid body reorientations with RDCs alone using Module (*29*) (N-TIMP-1 in blue) or RDCs plus intermolecular NOEs using XPLOR-NIH (*22*, *23*) (N-TIMP-1 in green). The coordinates of MMP-3(ΔC) (gold ribbon) of each model of the complex are superposed to show the differing orientations of bound N-TIMP-1. Secondary structure elements, loops, and termini are labeled. In MMP-3(ΔC), the zinc ions are pink, and calcium ions are light blue. The AB loop and β-strands A−D of TIMP-1 are in the foreground.

Table 1: Consistency of Structural Models of TIMP-Inhibited MMP Catalytic Domains with RDCs of MMP-3(ΔC)/N-TIMP-1 Complex in Solution[a]

	X-ray, MMP-3/TIMP-1[b]	RDC, MMP-3/N-TIMP-1	RDC + NOE, MMP-3/N-TIMP-1[c]	X-ray, MT1-MMP/TIMP-2[d]
rotation from MMP-3(ΔC)/ TIMP-1 X-ray[e] (deg)		+9	+5	+23
Q factor[f]	0.360	0.355	0.346	0.519[g]
RDC *R* factor[h] (%)	25.3	25.0	24.4	37.0[g]

[a] Using 121 RDCs comprising 96 $^1D_{NH}$ RDCs from N-TIMP-1 and 25 RDCs (18 $^1D_{NH}$ and 7 $^1D_{HC\alpha}$) from I/L/V-labeled MMP-3(ΔC). RDCs deviating from simulated RDCs by >21 Hz were omitted (i.e., from residues I19, R20, Q50, A55, R75, and I85 of N-TIMP-1 and L226 ($^1D_{HC\alpha}$) and I242 ($^1D_{NH}$) of MMP-3(ΔC)). Because of bad contacts introduced by protonation of the X-ray coordinates, eight iterations of unrestrained minimization using Sybyl 6.9 were used to decrease the bad contacts while limiting all-atom RMSD changes to less than 0.08 Å, without increasing *R* factors. [b] PDB coordinates 1uea, chains A and B. [c] PDB coordinates 1oo9 for apparent average orientation in solution. [d] PDB coordinate 1bqq. RDCs of MMP-3 were matched to MT1-MMP, and RDCs of N-TIMP-1 were matched to TIMP-2 using the structure-aided sequence alignment reported (*1*). [e] Rotation, relative to the fixed MMP orientation in 1uea, in the arc toward MT1-MMP/TIMP-2 orientation. [f] Defined as $RMS(RDC_{meas} - RDC_{pred})/RMS(RDC_{meas})$ by ref *54*. [g] Used 117 RDCs, primarily because of the shorter BC loop of TIMP-2. [h] Defined as $RMS(RDC_{meas} - RDC_{pred})/RMS(RDC_{random})$ where $RMS(RDC_{random}) = [2Da^2[4 + 3(Dr/Da)^2/5]]^{1/2}$, according to ref *55*.

similarity, the surface of MMP-3(ΔC) most protected from the broadening effects of Gd-EDTA when bound to N-TIMP-1 includes the amides from Asn162 through Ala167 and Ala169 encompassing β-strand IV (Figure 3A and Supporting Information Figure S2A). This is far more restricted and accurate set of interfacial residues than suggested by binding-linked chemical shift perturbations (*34*). The paramagnetic exclusion assay cannot assess binding-dependent occlusion of Ser206 because it is too recessed in the catalytic cleft. The NOE and paramagnetic protection results agree with changes in depth of amide groups of MMP-3(ΔC) below the surface accessible to a small paramagnetic probe in the absence and presence of N-TIMP-1 bound. Virtually the same set of residues undergo the greatest TIMP-1-binding-dependent burial from the paramagnetic probe-accessible surface (i.e., Asn162, Val163, Ala165, His166, Ala167, and Ala169 of the upper rim of the active site cleft (Supporting Information Figure S2B)). Ability to detect an N-TIMP-1-binding linked conformational change in MMP-3(ΔC) exposing its C helix (*34*) is an advantage of the paramagnetic protection assay over intermolecular NOEs. Where intermolecular NOEs are not available, interface mapping using chelated Gd(III) could sometimes provide a more accurate alternative to $^1H_N/^{15}N$ shift mapping for providing the ambiguous distance restraints for the translational component of protein−protein docking procedures that use RDCs (*24*, *45*).

Apparent Orientation of N-TIMP-1 in MMP-3(ΔC) Active Site with RDCs, Without and With NOEs. To determine the average global orientation of N-TIMP-1 in the active site of MMP-3(ΔC) in solution, the 102 most reliable RDCs were employed (i.e., those relatively free from picosecond to nanosecond and microsecond to millisecond dynamics). Pruning the deviant $^1D_{NH}$ measurements left 75 $^1D_{NH}$ values from N-TIMP-1 and 19 $^1D_{NH}$ plus eight $^1D_{H\alpha C\alpha}$ values from selectively labeled MMP-3(ΔC) bound. Reorientation using only RDCs used the program Module (*29*) to reconcile the independent alignment tensors of N-TIMP-1 and MMP-3(ΔC) (Figure S1 of Supporting Information), resulting in the orientation in Figure 4 with N-TIMP-1 in blue. With MMP-3(ΔC) superimposed, the backbone RMSD between X-ray structure (red in Figure 4) and the structure reoriented using only RDCs is 3.2 Å. Since the local RMSD systematically grows with distance from the interface, more meaningful is the angular difference of 9° between these models in red and blue in Figure 4. This rotation is in the arc toward the orientation in the crystal structure of MMP-3(ΔC) bound to TIMP-2. This RDC-based reorientation reconciles the 10°

discrepancy between the alignment tensors fitted to the two proteins in the crystal structure (Figure S1 of Supporting Information). The RDC-based reorientation (blue in Figure 4) agrees just slightly better with the RDCs in that its *Q* factor and *R* factor are slightly lower than those of the crystal structure (Table 1). To augment the orientation data from RDCs, the translational data of the 46 short distance contacts from intermolecular NOEs (Figure 2) were incorporated in rigid body docking using restrained simulated annealing in Cartesian space as described (*22*, *23*) using XPLOR-NIH (*43*). Interfacial residues 162−169, 198−202, 211, and 221−223 of MMP-3(ΔC) and residues 2, 4, 29, 33−35, and 66−69 of N-TIMP-1 were allowed flexibility in the otherwise rigid body docking. Inclusion or exclusion of the deviant $^1D_{NH}$ values (listed above) from docking using RDCs and NOEs with Cartesian simulated annealing (*22*, *23*) had scarcely any effect on the calculated orientation of MMP-3(ΔC) and N-TIMP-1 in complex. This suggests this rigid body docking protocol to be robust in the face of uncertainty in starting coordinates and in measured RDCs. This procedure with NOEs added resulted in a tight ensemble of structures with 25 of 25 calculated structures having an average global backbone RMSD of the N-TIMP-1 chain of 0.14 ± 0.10 Å (Supporting Information Figure S3). Their orientation is intermediate between the X-ray and the RDC-rotated orientations (i.e., 5° rotated from the crystal orientation in the same arc toward the MT1-MMP/TIMP-2 orientation). The lowest energy member of the tight ensemble is shown in green in Figure 4. This reorientation that supplemented the 102 RDCs with 46 intermolecular NOEs appears to be an enhancement over the X-ray or RDC-only orientations in that the *Q* and *R* factors are slightly better (Table 1). This structural model with enhanced agreement with the RDCs has been deposited in the PDB under accession code 1oo9.

This model has N-TIMP-1 rotated slightly toward the S-shaped calcium- and zinc-binding III−IV loop atop the *β*-sheet of MMP-3(ΔC) (at right in Figure 4). Comparing surface accessibility of this model with the X-ray model suggests N-TIMP-1 to be rotated slightly deeper into the S_3' subsite, mutually burying Val4 of N-TIMP-1 between Asn162 near *β*-strand IV and Tyr223 of MMP-3(ΔC) each a little deeper. Consistent with the importance of Val4 of N-TIMP-1 in MMP recognition, some mutations of Val4 can confer to engineered N-TIMP-1 greater selectivity among MMPs-1, 2, and 3 (*9*). In the solution model, the side chain of Val69 of the CD loop of N-TIMP-1 is also more buried in the heart of the interface. The intermolecular NOE-based distance restraints to the side chains of Val 4 and Val69 of N-TIMP-1 (Figure 2A) and to Asn162 and Tyr223 of MMP-3 (Figure 2B) allow the possibility that these residues could be more buried in solution.

Uncertainty, and its Sources, in Orientation of N-TIMP-1 in MMP-3 Active Site. From the apparent average orientation in solution resulting from use of both RDCs and NOEs, there is a 5° rotation back to the X-ray structure (red in Figure 4) and a 4° rotation ahead to the orientation based only on RDCs (blue in Figure 4). These latter two models agree with the RDCs almost as well as the intermediate orientation (Table 1). This suggests an uncertainty in the orientation of perhaps ±5° about the intermediate orientation (green in Figure 4) that is more realistic than the uncertainty of < ±1° suggested by the tight bundle of simulated annealing structures (Figure S3 of Supporting Information). Uncertainty in measured RDCs of ±1 Hz appears to result in uncertainty in the Euler angle to the principal axes of alignment of MMP-3(ΔC) and of N-TIMP-1 of ±1 and ±0.8°, respectively, based on simulated 1 Hz noise introduced into SVD fits (Figure S1 of Supporting Information). Error propagation then suggests around ±1.3° uncertainty in global orientation resulting from RDC measurement error. The 46 intermolecular NOEs and 75 RDCs of N-TIMP-1 seem ample and robust sources of experimental restraints, particularly as the orientation is insensitive to inclusion of outlying $^1D_{NH}$ values from N-TIMP-1. However, it is possible that availability of more than the 27 RDCs from the MMP-3(ΔC) backbone in the complex could decrease uncertainty in the global orientation. A larger source of the uncertainty in the global orientation is probably the structural uncertainty in the 2.8 Å crystal structure. Such uncertainty is manifest in the underestimated slopes in the RDC correlation plots of Figure 1B,C, in the underestimated Da measure of alignment (see above), and in the abundance of individual deviations between measured and calculated RDCs (Figure 1B,C). We have attributed most of the bigger deviations in N-TIMP-1 to dynamic averaging (*19*). Another viewpoint is to attribute the deviations to errors in the static X-ray coordinates.

If the 5° difference between the crystal orientation involving full-length TIMP-1 and the calculated solution orientation involving N-TIMP-1 were not subsumed by random uncertainties, there is a potential source of subtle, systematic structural difference. The absence of the C-terminal lobe from N-TIMP-1 and the resulting lack of contacts with loops to the right of the primed subsites of MMP-3 might permit it to rotate toward these loops. This would be in the observed direction toward the crystallographic orientation of TIMP-2 in the MT1-MMP active site (PDB code 1bqq). This might allow N-TIMP-1 to pivot more than full-length TIMP-1.

Possibility of Dynamic Pivoting of N-TIMP-1 in MMP-3 Active Site. The evidence of residual flexibility in the interface of the MMP-3(ΔC) complex with N-TIMP-1 suggests the possibility that slow dynamic averaging or pivoting of N-TIMP-1 in the active site of MMP-3(ΔC) in solution could also contribute to the range of uncertainty in their orientation in solution. Model-free results on backbone dynamics of N-TIMP-1 in the complex are available (BMRB code 5154) (*19*). S^2 of Thr2 of N-TIMP-1 in the interface being lower (0.85) than the average for the structured regions (0.92) is consistent with residual flexibility at this key site at the S_1' subsite in the heart of the interface. Exchange broadening evidence of fluctuations on the microsecond to millisecond scale throughout the MMP-binding ridge of N-TIMP-1 (i.e., at Thr2, Cys3, Cys70, of the CD loop and residues 29−36 of the AB loop) further suggests the possibility that this thin ridge slowly fluctuates while in the MMP active site (*19*). Deviations measured from predicted RDCs on the MMP-3(ΔC) side of the interface at Val198, Leu222, Leu226, and Leu229 (Figure 1B) could result from residual dynamic averaging in the primed subsites on the right side of the MMP-3 active site, especially around the central S_1' subsite. Again, residual flexibility in this region of the MMP-3 active site was reported in the backbone dynamics of MMP-3(ΔC) inhibited by small molecules (*50*).

Since RDCs fail to rule out the possibility in solution that N-TIMP-1 may pivot in the MMP-3(ΔC) active site in the arc of rotation defined by crystal structures of TIMP/MMP complexes, the range of possible orientations in solution was considered further. The RDCs measured from the complex of MMP-3(ΔC) with N-TIMP-1 were fitted to the X-ray coordinates of MTI-MMP(ΔC) with TIMP-2 bound (*53*) in an orientation rotated 23° about the active site relative to the MMP-3(ΔC)/N-TIMP-1 crystal structure (*20*), in the same arc as seen in Figure 4. The much higher *Q* and *R* factors of this fitting to the MTI-MMP(ΔC)/TIMP-2 coordinates (Table 1) suggest that this orientation is not compatible with RDCs of the MMP-3(ΔC)/N-TIMP-1 complex in solution. The RDC fittings to the structural models (Table 1) suggest that the MMP-3(ΔC)/N-TIMP-1 solution orientation is unlikely to sample orientations more than half the 18° rotation between the apparent average solution orientation of PDB code 1oo9 and that of the MTI-MMP(ΔC)/TIMP-2 crystal structure (PDB code 1bqq). Any possible time-averaged pivoting of N-TIMP-1 in the MMP-3(ΔC) active site would be limited to rotations of less than 9° by potential contacts of Lys88 of TIMP-1 with Arg149 and Asp158 of MMP-3 and of Gln90 of TIMP-1 with Pro156 of MMP-3(ΔC). Consequently, the N-TIMP-1 orientation in the MMP-3(ΔC) active site is unlikely to transiently swing within 10° of the TIMP-2 orientation in the MT1-MMP active site.

The differing orientations are unlikely to arise solely from skewing by artifacts of crystal packing. Crystal packing is more likely simply to freeze a TIMP into a favored low-energy orientation in an MMP active site. The disparity in TIMP-1 and TIMP-2 orientations observed by crystallography (*1*) now appears most likely to result from differences in the protein structure in the interfaces. The much longer extension of the AB loop of TIMP-2 that projects over the top of the β-sheet of MT1-MMP(ΔC) (*1*) is likely to push TIMP-2 further in the general direction of the primed subsites of the MMP (cf. Figure 4). Contact between the C-terminal lobe of TIMP-1 and the V−B loop of MMP-3(ΔC) (*20*), plus potential contacts involving Lys88 and Gln90 of TIMP-1, might resist the push in this direction.

In conclusion, the equivalence of the N-TIMP-1/MMP-3(ΔC) solution orientation with the TIMP-1/MMP-3(ΔC) crystallographic orientation, within experimental uncertainty, implies that the crystallographic models reliably represent the orientations in solution. It also implies that engineered N-TIMPs bind MMP catalytic domains very much like full-length TIMPs. The difference of 23° in TIMP-1/MMP-3(ΔC) and TIMP-2/MT1-MMP(ΔC) orientations is likely to result from inherent structural differences. The most obvious structural feature of short AB loops distinguishing TIMP-1 and TIMP-3 from the long AB loops of TIMP-2 and TIMP-4 may suffice to explain most of the range of orientations.

ACKNOWLEDGMENT

Q. Ye provided the plasmid to express wild-type human MMP-3 catalytic domain without prodomain (i.e., MMP-3(ΔC)). K. Brew provide the plasmid to express human N-TIMP-1. The NMR spectrometers at UMC were funded by NSF DBI0070359 for the 600 and NSF CHE8908304 for the 500, as well as by University of Missouri Research Board and Life Sciences Enhancement funding of the 600. NMRFAM provided DMX-750 time, F. Abildgard assisting. NHMFL provided access to the Unity+ 720. We thank G. M. Clore and co-workers for developing and distributing XPLOR-NIH and example scripts for protein−protein docking calculations. We thank R. Bhaskaran and G. Gao for critically reading this manuscript.

SUPPORTING INFORMATION AVAILABLE

Figure S1 showing alignment tensors fit to MMP-3(DC) and to TIMP-1 chains of PDB coordinate 1uea, Figure S2 comparing amide line broadening by Gd-EDTA with depth of amide, and Figure S3 showing ensemble of 25 models with N-TIMP-1 reoriented in MMP-3(ΔC) active site. This material is available free of charge via the Internet at http://pubs.acs.org.

REFERENCES

1. Fernandez-Catalan, C., Bode, W., Huber, R., Turk, D., Calvette, J. J., Lichte, A., Tschesche, H., and Maskos, K. (1998) *EMBO J. 17*, 5238−5248.
2. Murphy, G., and Willenbrock, F. (1995) *Methods Enzymol. 248*, 496−510.
3. Woessner, J. F., Jr., and Nagase, H. (2000) *Matrix metalloproteinases and TIMPs*, Oxford University Press, New York.
4. Khokha, R., Waterhouse, P., Yagel, S., Lala, P. K., Overall, C. M., Norton, G., and Denhardt, D. T. (1989) *Science 243*, 947−950.
5. Sternlicht, M. D., Lochter, A., Sympson, C. J., Huey, B., Rougier, J. P., Gray, J. W., Pinkel, D., Bissell, M. J., and Werb, Z. (1999) *Cell 98*, 137−146.
6. Williamson, R. A., Bartels, H., Murphy, G., and Freedman, R. B. (1994) *Protein Eng. 7*, 1035−1040.
7. Huang, W., Suzuki, K., Nagase, H., Arumugam, S., Van Doren, S. R., and Brew, K. (1996) *FEBS Lett. 384*, 155−161.
8. Meng, Q., Malinovskii, V., Huang, W., Hu, Y., Chung, L., Nagase, H., Bode, W., Maskos, K., and Brew, K. (1999) *J. Biol. Chem. 274*, 10184−10189.
9. Wei, S., Chen, Y., Chung, L., Nagase, H., and Brew, K. (2003) *J. Biol. Chem. 278*, 9831−9834.
10. Lee, M. H., Verma, V., Maskos, K., Nath, D., Knauper, V., Dodds, P., Amour, A., and Murphy, G. (2002) *Biochem. J. 364*, 227−234.
11. Butler, G. S., Hutton, M., Wattam, B. A., Williamson, R. A., Knauper, V., Willenbrock, F., and Murphy, G. (1999) *J. Biol. Chem. 274*, 20391−20396.
12. Williamson, R. A., Hutton, M., Vogt, G., Rapti, M., Knauper, V., Carr, M. D., and Murphy, G. (2001) *J. Biol. Chem. 4*, 4.
13. Stratmann, B., Farr, M., and Tschesche, H. (2001) *FEBS Lett. 507*, 285−287.
14. Muskett, F. W., Frenkiel, T. A., Feeney, J., Freedman, R. B., Carr, M. D., and Williamson, R. A. (1998) *J. Biol. Chem. 273*, 21736−21743.
15. Wu, B., Arumugam, S., Gao, G., Lee, G. I., Semenchenko, V., Huang, W., Brew, K., and Van Doren, S. R. (2000) *J. Mol. Biol. 295*, 257−268.
16. Gooley, P. R., O'Connell, J. F., Marcy, A. I., Cuca, G. C., Salowe, S. P., Bush, B. L., Hermes, J. D., Esser, C. K., Hagmann, W. K., Springer, J. P., and Johnson, B. A. (1994) *Nat. Struct. Biol. 1*, 111−118.
17. Williamson, R. A., Muskett, F. W., Howard, M. J., Freedman, R. B., and Carr, M. D. (1999) *J. Biol. Chem. 274*, 37226−37232.
18. Gao, G., Semenchenko, V., Arumugam, S., and Van Doren, S. R. (2000) *J. Mol. Biol. 301*, 537−552.
19. Arumugam, S., Gao, G., Patton, B. L., Semenchenko, V., Brew, K., and Van Doren, S. R. (2003) *J. Mol. Biol. 327*, 719−734.
20. Gomis-Rüth, F.-X., Maskos, K., Betz, M., Bergner, A., Huber, R., Suzuki, K., Yoshida, N., Nagase, H., Brew, K., Bourenkov, G. P., Bartunik, H., and Bode, W. (1997) *Nature 389*, 77−81.
21. Tjandra, N., and Bax, A. (1997) *Science 278*, 1111−1114.
22. Clore, G. M. (2000) *Proc. Natl. Acad. Sci. U.S.A. 97*, 9021−9025.
23. Wang, G., Louis, J. M., Sondej, M., Seok, Y. J., Peterkofsky, A., and Clore, G. M. (2000) *EMBO J. 19*, 5635−5649.

24. McCoy, M. A., and Wyss, D. F. (2002) *J. Am. Chem. Soc. 124*, 2104−2105.
25. Lukin, J. A., Kontaxis, G., Simplaceanu, V., Yuan, Y., Bax, A., and Ho, C. (2003) *Proc. Natl. Acad. Sci. U.S.A. 100*, 517−520.
26. Fischer, M. W., Losonczi, J. A., Weaver, J. L., and Prestegard, J. H. (1999) *Biochemistry 38*, 9013−9022.
27. Skrynnikov, N. R., Goto, N. K., Yang, D., Choy, W. Y., Tolman, J. R., Mueller, G. A., and Kay, L. E. (2000) *J. Mol. Biol. 295*, 1265−1273.
28. Mollova, E. T., Hansen, M. R., and Pardi, A. (2000) *J. Am. Chem. Soc. 122*, 11561−11562.
29. Dosset, P., Hus, J. C., Marion, D., and Blackledge, M. (2001) *J. Biomol. NMR 20*, 223−231.
30. Leeper, T. C., Martin, M. B., Kim, H., Cox, S., Semenchenko, V., Schmidt, F. J., and Van Doren, S. R. (2002) *Nat. Struct. Biol. 9*, 397−403.
31. Crabbe, T., Zucker, S., Cockett, M. I., Willenbrock, F., Tickle, S., O'Connell, J. P., Scothern, J. M., Murphy, G., and Docherty, A. J. (1994) *Biochemistry 33*, 6684−6690.
32. Windsor, L. J., Bodden, M. K., Birkedal-Hansen, B., Engler, J. A., and Birkedal-Hansen, H. (1994) *J. Biol. Chem. 269*, 26201−26207.
33. Steele, D. L., El-Kabbani, O., Dunten, P., Windsor, L. J., Kammlott, R. U., Crowther, R. L., Michoud, C., Engler, J. A., and Birktoft, J. J. (2000) *Protein Eng. 13*, 397−405.
34. Arumugam, S., Hemme, C. L., Yoshida, N., Suzuki, K., Nagase, H., Berjanskii, M., Wu, B., and Van Doren, S. R. (1998) *Biochemistry 37*, 9650−9657.
35. Van Doren, S. R., Kurochkin, A. V., Ye, Q. Z., Johnson, L. L., Hupe, D. L., and Zuiderweg, E. R. P. (1993) *Biochemistry 32*, 13109−13122.
36. Van Doren, S. R., Kurochkin, A. V., Hu, W. D., Ye, Q. Z., Johnson, L. L., Hupe, D. L., and Zuiderweg, E. R. P. (1995) *Protein Sci. 4*, 2487−2498.
37. Rückert, M., and Otting, G. (2000) *J. Am. Chem. Soc. 122*, 7793−7797.
38. Andersson, P., Weigelt, J., and Otting, G. (1998) *J. Biomol. NMR 12*, 435−441.
39. Ottiger, M., Delaglio, F., and Bax, A. (1998) *J. Magn. Reson. 131*, 373−378.
40. Clore, G. M., and Gronenborn, A. M. (1998) *Proc. Natl. Acad. Sci. U.S.A. 95*, 5891−5898.
41. Zweckstetter, M., and Bax, A. (2000) *J. Am. Chem. Soc. 122*, 3791−3792.
42. Fesik, S. W., and Zuiderweg, E. R. P. (1988) *J. Magn. Reson. 78*, 588−593.
43. Schwieters, C. D., Kuszewski, J. J., Tjandra, N., and Clore, G. M. (2003) *J. Magn. Reson. 160*, 65−73.
44. Schwieters, C. D., and Clore, G. M. (2001) *J. Magn. Reson. 152*, 288−302.
45. Clore, G. M., and Schwieters, C. D. (2003) *J. Am. Chem. Soc. 125*, 2902−2912.
46. Koenig, S. H., and Brown, R. D., III. (1990) *Prog. NMR Spectrosc. 22*, 487−567.
47. Nicholls, A., Sharp, K. A., and Honig, B. (1991) *Proteins 11*, 281−296.
48. Becker, J. W., Marcy, A. I., Rokosz, L. L., Axel, M. G., Burbaum, J. J., Fitzgerald, P. M. D., Cameron, P. M., Esser, C. K., Hagmann, W. K., Hermes, J. D., and Springer, J. P. (1995) *Protein Sci. 4*, 1966−1976.
49. Tolman, J. R., Flanagan, J. M., Kennedy, M. A., and Prestegard, J. H. (1997) *Nat. Struct. Biol. 4*, 292−297.
50. Yuan, P., Marshall, V. P., Petzold, G. L., Poorman, R. A., and Stockman, B. J. (1999) *J. Biomol. NMR 15*, 55−64.
51. Zweckstetter, M., and Bax, A. (2002) *J. Biomol. NMR 23*, 127−137.
52. Clore, G. M., Gronenborn, A. M., and Bax, A. (1998) *J. Magn. Reson. 133*, 216−221.
53. Fernandez-Catalan, C., Bode, W., Huber, R., Turk, D., Calvete, J. J., Lichte, A., Tschesche, H., and Maskos, K. (1998) *EMBO J. 17*, 5238−5248.
54. Cornilescu, G., Marquardt, J. L., Ottiger, M., and Bax, A. (1998) *J. Am. Chem. Soc. 120*, 6836−6837.
55. Clore, G. M., and Garrett, D. S. (1999) *J. Am. Chem. Soc. 121*, 9008−9012.

BI034545S